Key Engineering Materials
ISSN: 1662-9795, Vol. 1047, pp 105-113

Submitted: 2025-12-22
Revised: 2026-02-16
Accepted: 2026-02-25
Online: 2026-04-13

Numerical Study of the Flexural Behaviour of Additively Reinforced Blanks

Emanuele Fulco[1,a*], Pasquale Guglielmi[1,b], Angela Cusanno[2,c], Donato Sorgente[2,d]

[1]Department of Engineering, University of Basilicata, Potenza, Italy

[2]Department of Mechanics, Mathematics and Management – Politecnico di Bari, Bari, Italy

[a*]emanuele.fulco@unibas.it, [b]pasquale.guglielmi@unibas.it, [c]angela.cusanno@poliba.it, [d]donato.sorgente@poliba.it

*corresponding author: emanuele.fulco@unibas.it

Keywords: abaqus, bending, FEM, patchwork blanks, additive manufacturing.

Abstract. Tailored welded and patchwork blanks are commonly used in the automotive field to locally tailor the mechanical response of sheet metal components, but conventional manufacturing approaches often introduce structural discontinuities, corrosion-prone interfaces and limited formability. Additive deposition of local reinforcements offers a more flexible alternative, enabling material to be placed only where it provides the greatest structural benefit and reducing overall material usage and environmental impact. This work investigates the flexural behaviour of additively reinforced blanks through finite element simulations. A numerical model was developed in Abaqus to reproduce three-point bending tests on 22MnB5 sheets locally reinforced by the wire-laser additive deposition of a 316L stainless steel. Metallographic cross-sections were used to define the reinforcement geometry and penetration depth, micro-hardness profiles to define the extent of the heat affected zone, and plastometric characterisation to obtain local mechanical properties. The simulations demonstrate that the proposed numerical model reliably reproduces the experimentally observed flexural behaviour of wire-laser additively reinforced blanks. The numerical force-displacement response is consistent with the experimental one, and within this agreement the increase in bending strength obtained with minimal added material is confirmed.

Introduction

Lightweight design is a key strategy for reducing emissions in the automotive field and supporting the wider transition toward low-carbon mobility. Reducing the mass of structural components directly lowers energy demand and CO_2 emissions for both conventional and electrified vehicles [1–4], while offering immediate benefits that complement long-term decarbonisation efforts [5]. Given that sheet-metal manufacturing contributes significantly to the total energy and material footprint of vehicle production [6], improving material efficiency has become a central objective. Additive and hybrid manufacturing approaches have therefore gained increasing attention due to their potential to reduce waste, enhance resource efficiency and support the development of optimised lightweight structures [7,8]. A widely adopted solution for achieving lightweight construction involves tailoring the local properties of sheet-metal components. Traditional solutions such as tailored welded blanks, tailored rolled blanks, tailored heat treated blanks and patchwork blanks seek to reinforce only the most critical regions while avoiding unnecessary mass [9–12]. However, conventional joining-based approaches may introduce structural discontinuities, corrosion-susceptible interfaces and reduced formability during downstream processing, limiting their applicability in advanced automotive manufacturing. Additive deposition presents an appealing alternative, enabling the placement of reinforcement material with high spatial precision while reducing waste and supporting sustainability goals [6–8,13]. Recent contributions in hybrid manufacturing further highlight the potential of integrating additive strategies with established forming processes [14–16]. Experimental studies on wire-laser additively reinforced blanks have also shown that the additive deposition of metallic tracks can significantly increase bending strength while requiring only minimal additional material, thereby

improving the efficiency of patchwork-style reinforcements [17]. Despite this progress, the literature on additively reinforced sheet-metal blanks has primarily emphasised microstructural or material characterisation, whereas systematic evaluations of their mechanical performance, especially under bending loads relevant to automotive components, remain limited.

To support the industrial adoption of additively reinforced blanks, it is essential to rely on predictive tools that can relate the geometry of the reinforcement, its penetration into the substrate and the resulting material response to the overall structural behaviour of the component. Bending is a relevant loading condition for sheet-metal applications, as it is highly sensitive to local stiffness variations and therefore provides a direct measure of reinforcement effectiveness. In this context, the aim of the present work is to develop a numerical model capable of reproducing the flexural behaviour observed experimentally in additively reinforced blanks [17]. The model, implemented in Abaqus, incorporates reinforcement geometry and penetration depth obtained from optical microscopy, while the mechanical properties assigned to the base material, the heat affected region and the deposited metal reinforcement (fused zone) are derived from non-destructive Profilometry-Indentation Plastometry (PIP). By comparing numerical predictions with experimental measurements, the study investigates the reliability of the proposed model in capturing the flexural response of the investigated specimens.

Material and Methods

Additive Deposition and Material Characterisation.

To develop a finite element model with realistic and spatially differentiated material properties, an initial experimental characterisation campaign was carried out on physically manufactured specimens. Steel sheets of 22MnB5 were reinforced by the wire-additive deposition of two parallel 316L tracks, each 20 mm in length and spaced 1 mm apart. The deposition was performed using a Meltio M350 system, under constant processing conditions to ensure repeatability across samples. The system employs six 200 W diode lasers, angled at 25°, with a 976 nm wavelength. Following deposition, the reinforced sheet was cut into specimens of 80 × 20 mm. A schematic representation of the wire-laser additive deposition setup used in this study is shown in Fig. 1.

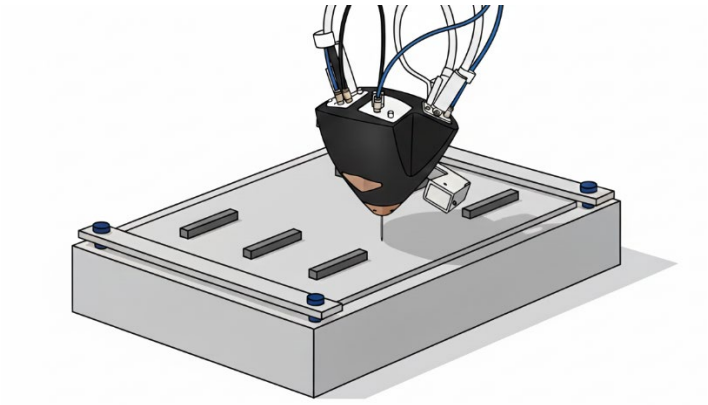

Fig. 1. Schematic representation of the wire-laser additive deposition setup, showing the clamped 22MnB5 sheet and the local reinforcement obtained by depositing parallel 316L wire tracks.

Each specimen was subsequently hot-mounted using ConduFast® resin at 180 °C and 250 bar, with a heating time of 3.5 minutes followed by 1.5 minutes of cooling. Then, they were polished and chemically etched to reveal the fused zone (FZ) and the surrounding heat affected zone (HAZ) in the cross-section. These cross-sectional analyses provided quantitative measurements of the reinforcement geometry, including bead height, width and penetration depth into the substrate. To determine the local mechanical response of the different regions, plastometric tests were carried out using a PLASTOMETREX PLX-Benchtop system, which implements the Profilometry-based Indentation Plastometry (PIP) technique. Indentations were performed in the three zones of interest, namely the Base Material (BM), the Heat Affected Zone (HAZ), and the Fused Zone (FZ)

corresponding to the deposited reinforcement. A spherical indenter with a diameter of 0.5 mm was employed, with an indentation velocity of 4 μm/s and a maximum indentation depth of approximately 90 μm, in order to probe the plastic response while maintaining the deformation in a predominantly localised regime. For each indentation, the applied load-displacement data and the three-dimensional imprint geometry, acquired by profilometry, were processed through the CORSICA software supplied with the PLX system. By means of an inverse analysis procedure, CORSICA identifies the constitutive parameters that best reproduce the measured response, providing the corresponding true stress-strain curve for the tested material point. In this work, the plastic portion of the response was approximated by a Voce-type hardening law, which was calibrated separately for the BM, HAZ, and FZ. The resulting geometric and constitutive data for the three regions were then used as input for the numerical model developed to simulate the bending test on the reinforced specimen.

Numerical Modelling.

Finite element simulations were performed in Abaqus to replicate a three-point bending test on the reinforced sheet. For reference and comparison purposes, an additional simulation was also performed on a flat, unreinforced sheet, modelled entirely as BM. Three analytical rigid bodies were introduced to represent the punch and the two anvils, reproducing the experimental bending configuration. In order to ensure numerical robustness while limiting model complexity, the finite element model was constructed by introducing a set of simplifying assumptions, which are explicitly referenced throughout the following description. The specimen was represented as a deformable three-dimensional solid and, to reduce the computational cost, (i) the model was reduced to one quarter of the full geometry by assuming the reinforcement bead to be symmetric with respect to both the longitudinal and transverse directions. Appropriate symmetry boundary conditions were applied on the corresponding planes. The specimen was partitioned to distinguish the reinforcement (FZ) from the sheet metal substrate. (ii) The cross-section of the reinforcement was simplified with respect to the real deposited morphology and modelled as a portion of an ellipse, as shown in Fig. 2a and 2b, whose major axis corresponds to the average reinforcement width (3.66 mm) and whose height (0.81 mm) matches the average reinforcement height measured at a deposition power of 1100 W, as reported in a previous study [17].

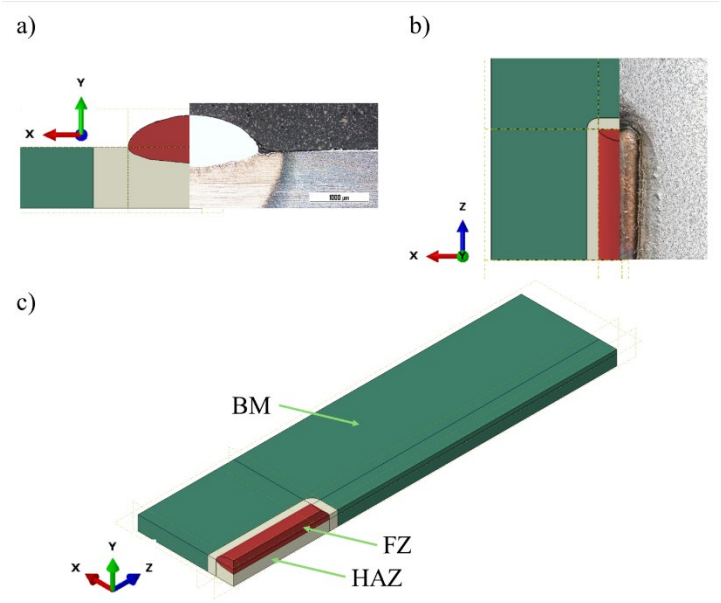

Fig. 2. Experimental geometry of the reinforced sheet and corresponding numerical representation. (a) Cross-section view showing the experimental reinforcement profile and its elliptical representation, together with the heat affected zone (HAZ) modelled with a straight-through-thickness simplified geometry. (b) Top view highlighting the simplified geometry adopted for the reinforcement and the HAZ. (c) Partitioned geometry adopted in the numerical model, showing the base material (BM), heat affected zone (HAZ) and fusion zone (FZ).

This representation was adopted to retain the dominant geometric features of the reinforcement while avoiding unnecessary geometric complexity. A second partition was introduced around the reinforcement to represent the heat affected zone (HAZ). (iii) The HAZ was modelled as a region extending through the sheet thickness with straight boundaries, as shown in Fig. 2a and 2b, meaning that the characteristic cup-shaped morphology observed experimentally in cross-section was not explicitly reproduced. The in-plane width and longitudinal extent of the HAZ were instead defined on the basis of experimental hardness maps, obtained using a Qness 10A+ tester by applying a load of 0.2 kg (HV0.2) in accordance with ASTM E-384, with a dwell time of 15 s. Accordingly, a uniform HAZ extension of 0.86 mm around the reinforcement was adopted. Within the numerical model, BM, HAZ and FZ were defined as distinct material regions, as shown in Fig. 2c. Each region (iv) was assumed to be mechanically homogeneous, and was therefore assigned a single constitutive description, derived from the corresponding plastometric characterisation discussed in the previous section. Although property gradients are known to develop within both the HAZ and the FZ in the real component, this simplification was adopted to preserve a clear mechanical distinction between regions while maintaining a manageable model complexity. All these assumptions also allowed to preserve a structured mesh in the discretization of the deformable body and to have a fast and reliable measurement strategy in the PIP tests. At the same time, these assumptions are not expected to significantly affect the global response of the specimen, in particular the macroscopic force-displacement behaviour under three-point bending. Contact interactions were defined between the punch, anvils and specimen, using a coefficient of friction equal to 0.20. The three-point bending test was simulated by imposing a downward displacement of 12 mm to the punch under displacement-controlled conditions, consistently with the experimental setup reported in a previous work [17].

The boundary conditions were defined consistently with the adopted symmetry assumptions and the experimental bending setup. The two anvils were fully constrained by applying an encastre condition at their respective reference points. During the bending step, the punch was allowed to move exclusively along the vertical direction, while all remaining degrees of freedom were constrained, ensuring a controlled kinematic loading. Symmetry boundary conditions were applied to the quarter model of the reinforced sheet to reproduce the full geometry behaviour. A symmetry constraint was imposed on the plane normal to the longitudinal direction (Z-axis), and a second symmetry constraint was applied on the plane normal to the transverse direction (X-axis). These constraints enforce zero displacement normal to the symmetry planes and prevent spurious rigid-body motion, ensuring that the deformation of the quarter model remains mechanically equivalent to that of the full specimen under symmetric loading conditions.

The punch and the anvils were modelled as discrete rigid bodies and discretised using four-node three-dimensional rigid elements (R3D4), with a uniform element size of 0.5 mm, as illustrated in Fig. 3a. The sheet was instead discretised as a deformable body using eight-node three-dimensional brick elements with reduced integration (C3D8R). As shown in Fig. 3b and 3c, a non-uniform mesh was adopted: an average element size of 0.5 mm was used in the BM region, a refined discretisation with an element size of 0.2 mm was applied within the HAZ, and a further refinement to 0.1 mm was introduced in the FZ beneath the punch, where the highest bending strains were expected.

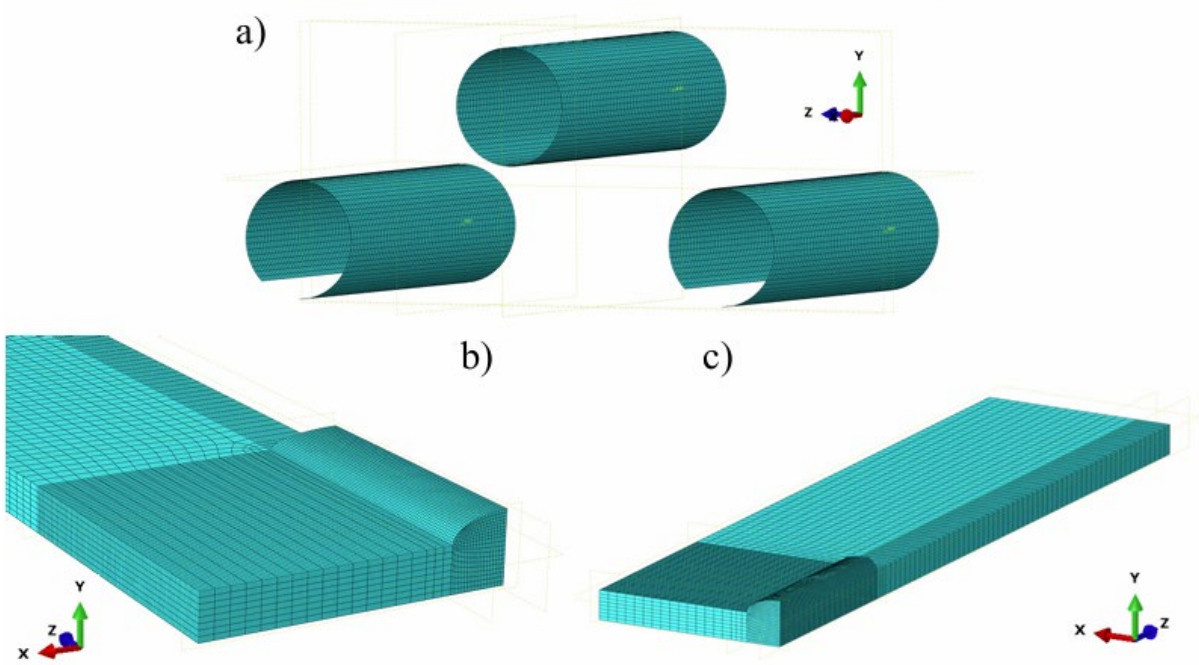

Fig. 3. Finite element discretisation of the numerical model: (a) mesh of the 3D discrete rigid punch and supports (R3D4); (b) mesh of the 3D deformable reinforced sheet (C3D8R), showing the HAZ and the local refinement in the FZ beneath the punch; (c) global view of the same mesh highlighting the coarsening towards the specimen ends.

This meshing strategy allowed the local flexural response to be captured accurately while keeping the overall computational cost under control. All simulations were performed using Abaqus on a workstation equipped with an Intel Xeon W7-3465X processor, 256 GB of RAM. For the adopted mesh density and modelling assumptions, a complete three-point bending simulation required approximately 30 min of computation time.

Results and Discussion

As reported in the previous sections, plastometry tests were used to characterise the mechanical response of the three material regions composing the reinforced sheet, namely BM, HAZ and the reinforcement (FZ). Fig. 4 shows the resulting true stress-true plastic strain curves of the three regions. The BM exhibits the lowest flow stress with values that are in agreement with those that can be found in literature for the as-received 22MnB5 steel [18]. The FZ displays a significantly higher strength level (up to about 1500 MPa), while the HAZ shows the highest flow stress (up to about 1760 MPa), particularly at low plastic strains, indicating a marked strengthening induced by the thermal cycle of the laser additive reinforcement process. The different hardening responses highlight the presence of strong local mechanical gradients across the sheet. These results support the modelling approach adopted in this work, in which BM, HAZ and FZ are treated as mechanically distinct regions for the numerical simulation of the three-point bending test.

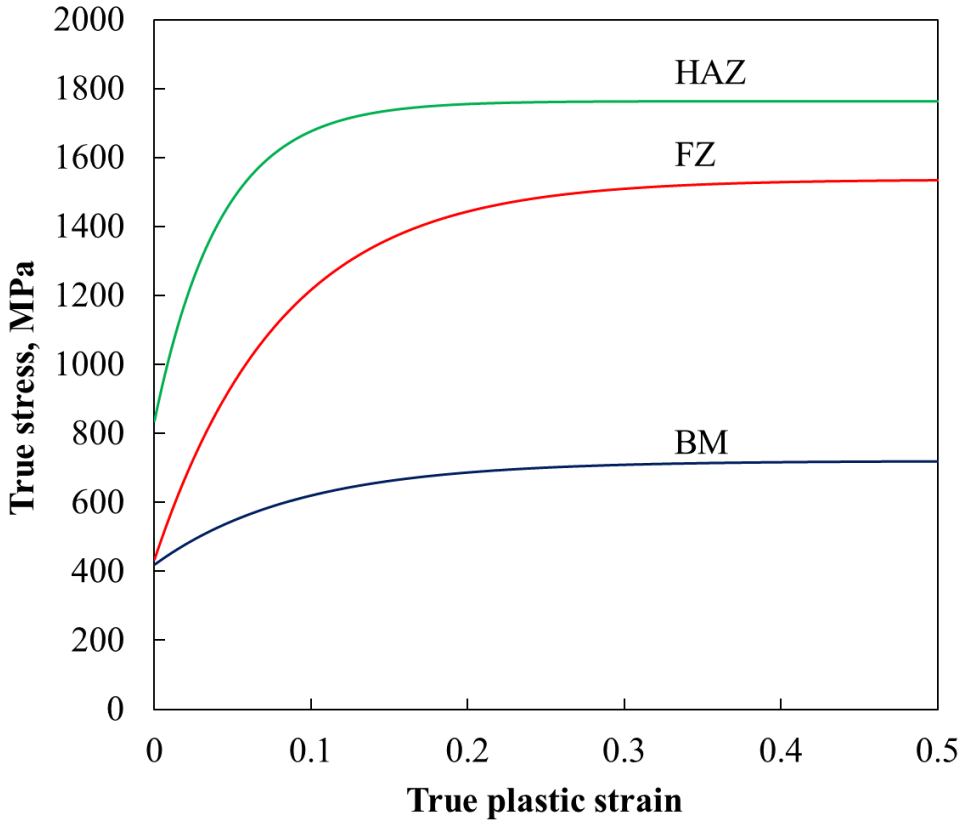

Fig. 4. True stress-true plastic strain curves obtained from plastometry for the base material (BM), the heat affected zone (HAZ) and the reinforcement (FZ) of the additively reinforced sheet.

Fig. 5 illustrates the time evolution of the bending simulation in terms of equivalent plastic strain (PEEQ). The sequence clearly shows a through-thickness strain distribution, with tensile fibres developing at the outer surface (extrados) and compressive fibres at the inner surface (intrados), separated by a well-defined neutral line.

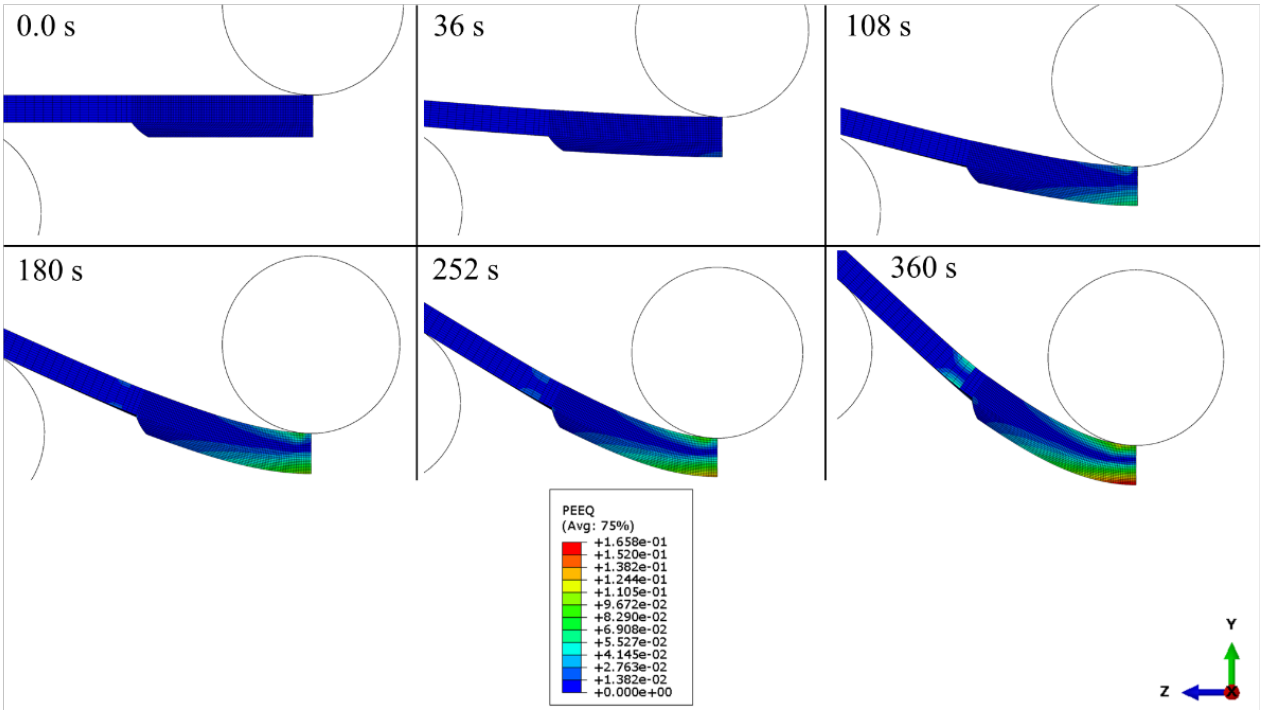

Fig. 5. Time evolution of the bending simulation shown in terms of equivalent plastic strain (PEEQ) at selected time instants.

The maximum PEEQ value (0.1658) occurs at the top of the reinforcement at the specimen mid-span, where the bending moment is maximum. Plastic deformation remains mainly localised in the bending region throughout the process. In Fig. 6, a comparison between the experimental and numerical force-displacement curves is presented. To improve readability, the experimental repetitions for each condition are represented using a consistent colour scheme and condensed into a single legend label. The numerical force-displacement curves reproduce the trend of the experimentally obtained curves, both in terms of slope and force levels. For the 1100 W condition, the numerical curve slightly overestimates the experimental response in the mainly elastic region and slightly underestimates it in the plastic regime, where five out of the six experimental curves lie above the numerical prediction and only one falls below it (Fig. 6). These small deviations are probably related to the geometric simplifications adopted in the model, since the reinforcement profile observed experimentally is imperfect due to the deposition process and not completely symmetric (Fig. 2), which can reasonably explain the small shifts observed in the force-displacement curve. Furthermore, numerical parameters, such as mesh density and friction coefficient, are not expected to be the primary causes of these deviations, given that the same configuration applied to the unreinforced condition provided an excellent fit with the experimental data. Indeed, for both the base material and the reinforced condition, the numerical results lie within the range defined by the experimental curves throughout the bending process. In this context, in a previous work [17] the authors reported that, for the 1100 W condition, a mass increase of 1.6% for the specimen corresponds to an increase in maximum bending force of 82.2% with respect to the base material; this quantitative trend is consistently reflected by the positioning of the numerical force-displacement curve in Fig. 6. This outcome is particularly relevant for the reinforced specimens, where geometric and material simplifications were introduced in the numerical model, including symmetry assumptions, simplified representations of the reinforcement and the heat affected zone, and the definition of mechanically homogeneous material regions. Despite the absence of material property gradients within the HAZ and the FZ, the numerical response remains close to the experimental one, indicating that these assumptions do not significantly affect the predicted bending behaviour.

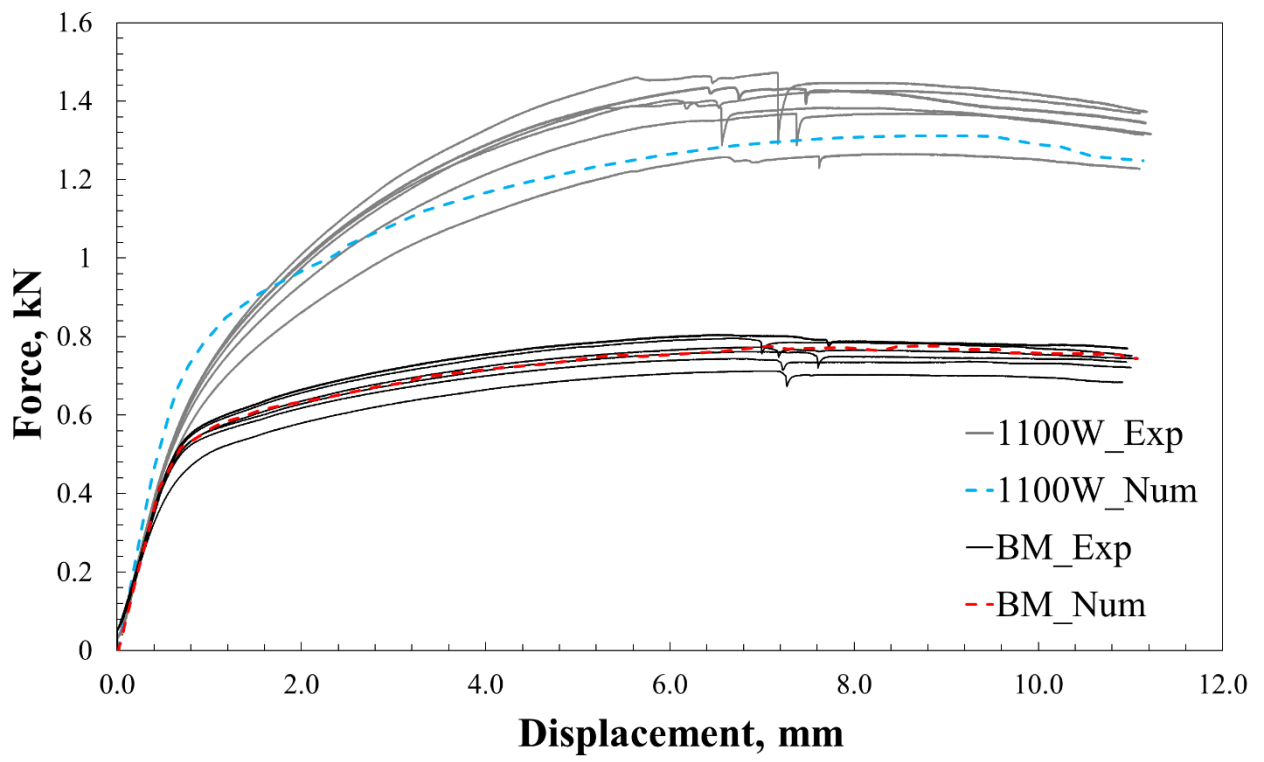

Fig. 6. Comparison between experimental and numerical force-displacement curves for the base material (BM) and the reinforced condition (1100 W).

Conclusion

A finite element model was developed to predict the flexural behaviour, under three-point bending, of wire-laser additively reinforced 22MnB5 blanks with a 316L stainless steel reinforcement. The reinforcement geometry was defined from metallographic cross-sections, while the mechanical properties of the base material (BM), the heat affected zone (HAZ) and the deposited material (FZ) were obtained by Profilometry-based Indentation Plastometry (PIP). The numerical force-displacement curves obtained with the model fall within the experimental results for both reinforced specimens and unreinforced 22MnB5 sheets. This shows that, despite the adopted geometric and constitutive simplifications, the numerical approach reliably predicts the bending behaviour of the investigated configurations. Future work will focus on extending the model to incorporate property gradients within the HAZ and FZ, with the aim of eliminating the artificial local strain discontinuities observed in the current model and obtaining a more accurate estimation of the neutral-layer position during bending while also exploring multi-layer reinforcements.

References

[1] C. Fetting, “The European Green Deal”, ESDN Report, Eur. Comm. 53 (2020) 24. https://eur-lex.europa.eu/legal-content/EN/TXT/PDF/?uri=CELEX:52019DC0640&from=EN.

[2] Jan Dornoff, CO2 emission standards for new passenger cars and vans in the European Union, (2023). https://theicct.org/publication/eu-co2-standards-cars-vans-may23/.

[3] G. Çınar, THE GREEN DEAL AND THE AUTOMOTIVE INDUSTRY IN THE EU Transforming the Automotive Industry-Impact on EU Regions, (2020). https://reneweurope-cor.eu/wp-content/uploads/2020/06/The-Green-Deal-and-the-Automotive-Industry-in-the-EU.pdf.

[4] A. Cimprich, K. Sadayappan, S.B. Young, Lightweighting electric vehicles: Scoping review of life cycle assessments, J. Clean. Prod. 433 (2023) 139692. https://doi.org/10.1016/j.jclepro.2023.139692.

[5] A.C. Serrenho, J.B. Norman, J.M. Allwood, The impact of reducing car weight on global emissions: The future fleet in Great Britain, Philos. Trans. R. Soc. A Math. Phys. Eng. Sci. 375 (2017). https://doi.org/10.1098/rsta.2016.0364.

[6] P.M. Horton, J.M. Allwood, Yield improvement opportunities for manufacturing automotive sheet metal components, J. Mater. Process. Technol. 249 (2017) 78–88. https://doi.org/10.1016/j.jmatprotec.2017.05.037.

[7] J. Lessard, L. Darunte, S. Jayanathan, Decarbonizing Structural Alloys in Consumer Electronics : Case Studies at Apple, J. Sustain. Metall. 11 (2025) 3550–3563. https://doi.org/10.1007/s40831-025-01258-1.

[8] C. Gao, S. Wolff, S. Wang, Eco-friendly additive manufacturing of metals: Energy efficiency and life cycle analysis, J. Manuf. Syst. 60 (2021) 459–472. https://doi.org/10.1016/j.jmsy.2021.06.011.

[9] E. Cischino, F. Di Paolo, E. Mangino, D. Pullini, C. Elizetxea, C. Maestro, E. Alcalde, J.D. Christiansen, An Advanced Technological Lightweighted Solution for a Body in White, Transp. Res. Procedia 14 (2016) 1021–1030. https://doi.org/10.1016/j.trpro.2016.05.082.

[10] H. Kusuda, T. Takasago, F. Natsumi, Formability of tailored blanks, J. Mater. Process. Technol. 71 (1997) 134–140. https://doi.org/10.1016/S0924-0136(97)00159-3.

[11] K. Lamprecht, M. Geiger, Characterisation of the forming behaviour of patchwork blanks, Steel Res. Int. 76 (2005) 910–915. https://doi.org/10.1002/srin.200506115.

[12] K. Lamprecht, M. Merklein, M. Geiger, Hydroforming of patchwork blanks - Numerical modeling and experimental validation, AIP Conf. Proc. 778 A (2005) 526–531. https://doi.org/10.1063/1.2011274.

[13] K. Sathish, S.S. Kumar, R.T. Magal, V. Selvaraj, V. Narasimharaj, R. Karthikeyan, G. Sabarinathan, M. Tiwari, A.E. Kassa, A Comparative Study on Subtractive Manufacturing and Additive Manufacturing, Adv. Mater. Sci. Eng. 2022 (2022). https://doi.org/10.1155/2022/6892641.

[14] M.A. Rabalo, E.M. Rubio, B. Agustina, A.M. Camacho, Hybrid additive and subtractive manufacturing: Evolution of the concept and last trends in research and industry, Procedia CIRP 118 (2023) 741–746. https://doi.org/10.1016/j.procir.2023.06.127.

[15] H. Dardaei Joghan, R. Hölker-Jäger, A. Komodromos, A.E. Tekkaya, Hybrid Additive Manufacturing of Forming Tools, Automot. Innov. 6 (2023) 311–323. https://doi.org/10.1007/s42154-023-00239-y.

[16] Mapping the future with 3D-printed titanium Apple Watch cases - Apple, (n.d.). https://www.apple.com/newsroom/2025/11/mapping-the-future-with-3d-printed-titanium-apple-watch-cases/ (accessed November 26, 2025).

[17] E. Fulco, D. Sorgente, Wire laser additively reinforced blanks: effect of the laser power on the bending strength of a single layer reinforcement, J. Mater. Res. Technol. 33 (2024) 1276–1285. https://doi.org/10.1016/j.jmrt.2024.09.036.

[18] Press Hardening Steel Grades - AHSS Guidelines, (n.d.). https://ahssinsights.org/metallurgy/steel-grades/phs-grades/ (accessed December 18, 2025).